REPORT DOCUMENTATION PAGE

AFRL-SR-BL-TR-00-

0307

1. AGENCY USE ONLY *(Leave blank)*	2. REPORT DATE	3.
	May 9, 2000	* Final March,1996-July,1999

4. TITLE AND SUBTITLE	5. FUNDING NUMBERS
Thermomechanical Behavior of Functionally Graded Materials	F49620-96-1-1058 0158

6. AUTHOR(S)

A. Almajid, S. Hudnut and M. Taya

7. PERFORMING ORGANIZATION NAME(S) AND ADDRESS(ES)

Center for Intelligent Materials and Systems
Department of Mechanical Engineering
University of Washington, Box 352600
Seattle, WA 98195-2600

8. PERFORMING ORGANIZATION REPORT NUMBER

9. SPONSORING/MONITORING AGENCY NAME(S) AND ADDRESS(ES)

Air Force Office of Scientific Research
Directorate of Aerospace and Material Sciences
AFOSR/NA
801 N. Randolph Road, Room 732
Arlington, VA 22203-1977

10. SPONSORING/MONITORING AGENCY REPORT NUMBER

11. SUPPLEMENTARY NOTES

12a. DISTRIBUTION AVAILABILITY STATEMENT

unlimited

20000727 217

13. ABSTRACT *(Maximum 200 words)*

Functionally graded materials are studied with emphasis on fracture resistance behavior and piezoelectric performance. Several types of metal/ceramic FGM plates are processed and their fracture resistance, Kr as a function of crack length was examined experimentally. The Kr behavior of the FGM plates are explained by two models successfully.

Then, a new type of piezoelectric FGM plates are designed by using several models, classical lamination theory, 2D elasticity model and FEM. Based on these models, the optimum microstructure of the FGM layering was identified, leading to larger out-of-plane displacement under the applied electric field, while minimizing the induced stress field, thus, enhancing its fatigue life. The optimum microstructure of the FGM is composed of a number of composite layers(laminae) through the plate thickness such that the top half layering is symmetric with respect to the mid-plane where the electrodes are located at the top, bottom as well as in the mid-plane.

Based on the above optimization of the FGM layering, we designed a FGM laminate plate where each lamina consists of continuous piezo fiber composite, and performed rigorous FEM analysis. Finally, concluding remarks and future works are given.

14. SUBJECT TERMS	15. NUMBER OF PAGES
	30
	16. PRICE CODE

17. SECURITY CLASSIFICATION OF REPORT	18. SECURITY CLASSIFICATION OF THIS PAGE	19. SECURITY CLASSIFICATION OF ABSTRACT	20. LIMITATION OF ABSTRACT
unclassified			

DTIC QUALITY INSPECTED 4

Table of contents

1.   Processing Ni/Al$_2$O$_3$ and Ni/ZrO$_2$ FGMs

Residual stresses are developed in metal-ceramic interface during cooling as a result of the property mismatch across the bonded interface. The design of the spatial variation of the FGM needed to be optimized to minimize the thermal stresses that can cause joint failure during fabrication or while in service. The optimized variation was considered for fabrication based on amount of stress reduction and on the ease of fabrication. Powder processing techniques are suited for fabrication of gradient materials because of the tremendous microstructural control and versatility inherent on them. Two powder metallurgical routes were considered, tape casting method and powder compaction. Tape casting method was used for the processing thin films. The material system was chosen to represent both ceramic and metal. Al$_2$O$_3$ and ZrO$_2$ represent high temperature materials and Ni represents nickel alloys system that is extensively used in aerrspace engines and their characteristics are presented in Table 1.

Ni/Al$_2$O$_3$ specimens were processed using tape casting method while Ni/ZrO$_2$ specimens were processed using powder compaction method. The processing route is schematically shown in Figure 1. The amount of deflouculant, solvent, binder, and plasticizer have to be carefully chosen to provide a strong and flexible tapes. A trial and error procedure took place to achieve strong and flexible tapes prior to hot press. Table 2 shows the formulation of one of the layers, 100% Al$_2$O$_3$. The tapes were casted using stationary doctor blade machine as shown in Figure 2 to minimize vibrations associated with moving blade which would alter the thickness consistency of the tapes. The ceramic and metal powders were mixed together for each volume fraction. Wet mixing was used and by the use of sonic waves, homogenous materials were established. In the case of the die compaction, the pressure needed to be applied to the powder so not to have pre-cracking in the material was investigated.

Characteristics	Nickel	Al$_2$O$_3$	ZrO$_2$
Vendor	INCO	Alcoa	Zirconia Inc.
purity %	99.7	99.9	94
Avg. particle size, μm	1-5	0.5	0.5- 25
Major impurities %	O$_2$ 0.15	Na$_2$O 0.006	Y$_2$O3 4-6

Table 1 Powder Characteristics

Material	Weight (gm)
Al$_2$O$_3$	40
Glycerol	2.53
PEG	0.78
Ethanol	32
H2O	33
Binder	1.29

Table 2 formulation for tape casting

Figure 1 flowcharts

(a) Tape casting method

```
Material   Material   Deflocculan   Solvent
                  |
              Ball Mill
Binder ——     Mix     —— Plasticizer
              De-air
              Filter
             Tape cast
           Stacking tapes
           Cold isostatic
           Burn off binder
            Hot press at
```

(a)

(b) Powder pressing method

```
         Wet mixing
          drying
       Die compaction
     Sintering at 1275C
    HIP in Argon at 1275C
```
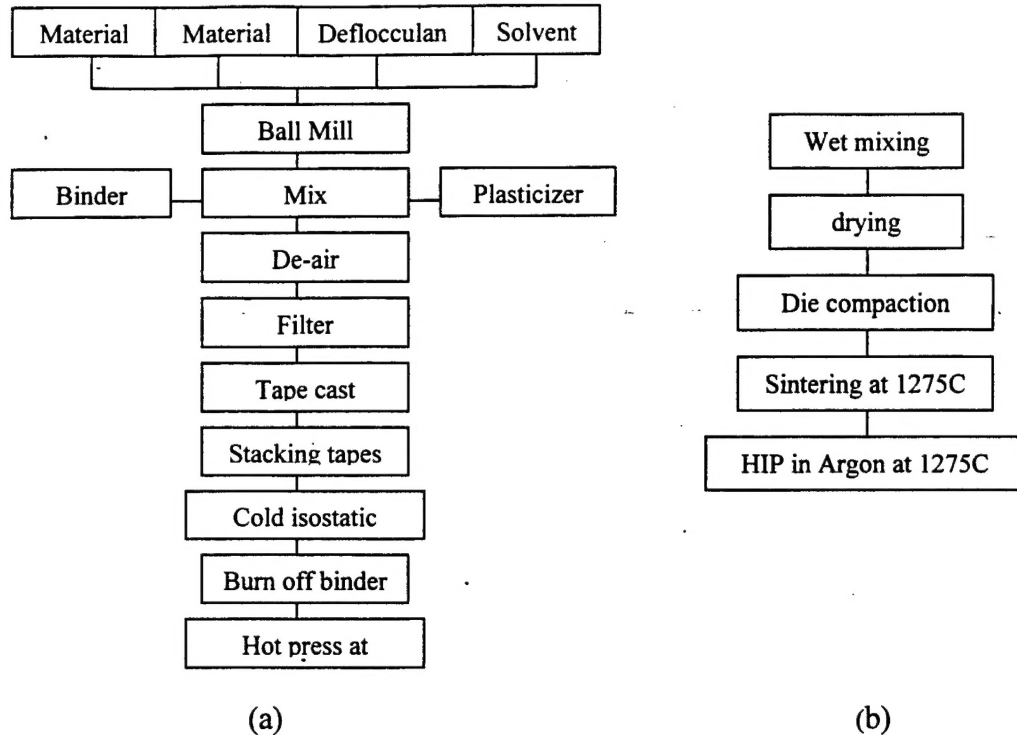
(b)

Figure 1 processing route of FGM, (a) tape casting method.,
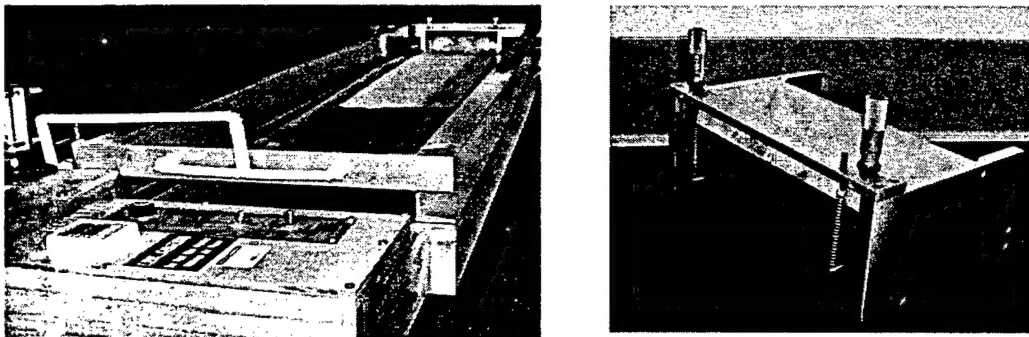(b) powder pressing method

Figure 2 Tape casting machine and
Doctor blade assembly

Ni/ ZrO_2 with two different ZrO_2 particle sizes were processed. The two processed FGMs are 3.6 μm Ni, 25 μm ZrO_2, and 3.6 μm Ni, 0.2 μm ZrO_2. After successful processing of FGM, sectional microstructure views of the Ni/ ZrO_2 sample were obtained by optical microscope and are shown in Figure 3 for the 3.6 μm Ni, 25 μm ZrO_2 system and Figure 4 for the 3.6 μm Ni, 0.2 μm ZrO_2 system, where the white and dark domains are metal and ceramic phases, respectively. The microstucrture was analyzed for damaged and debonding associated with particles. Once the system is analyzed and approved, then experimental samples are processed. This was to assure the quality and reproducibility of the FGM samples.
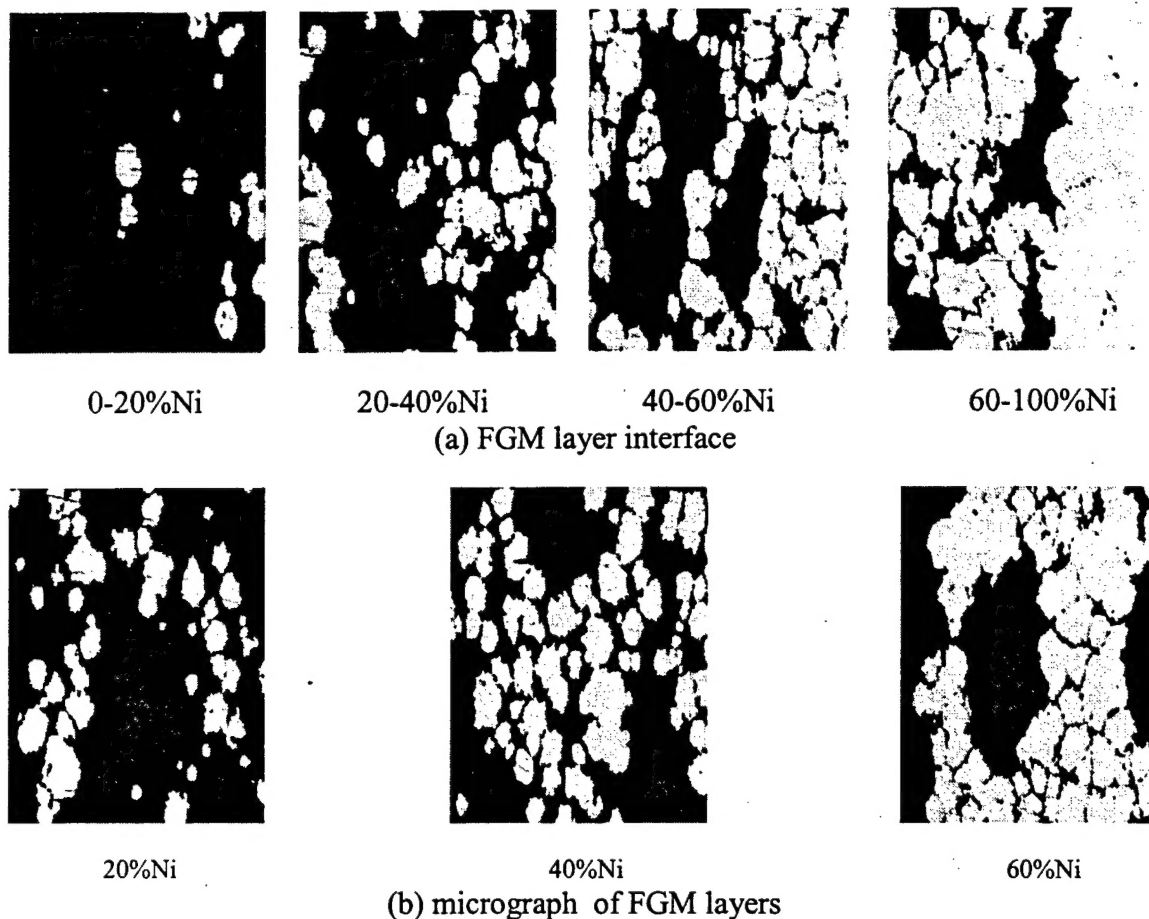
| 0-20%Ni | 20-40%Ni | 40-60%Ni | 60-100%Ni |

(a) FGM layer interface

| 20%Ni | 40%Ni | 60%Ni |

(b) micrograph of FGM layers

Figure 3 Optical micrograph of metal /ceramic Ni/ZrO_2 with 3.6 μm Ni, 25 μm ZrO_2 system FGM layers (a) FGM layer interface, (b) micrograph of FGM layers

In Figure 3, the 3.6 μm Ni, 25 μm ZrO_2 FGM consists of five layers starting from 0%Ni to 100%Ni in an increment of 20%. Figure 3(a) shows the interface between the layers which are bonded well to each other as no cracks visible under a microscope. As the volume fraction increases, the Ni phase starts to agglomerate under diffusion. For that reason, islands of Nickels were found in high volume fraction of Ni.
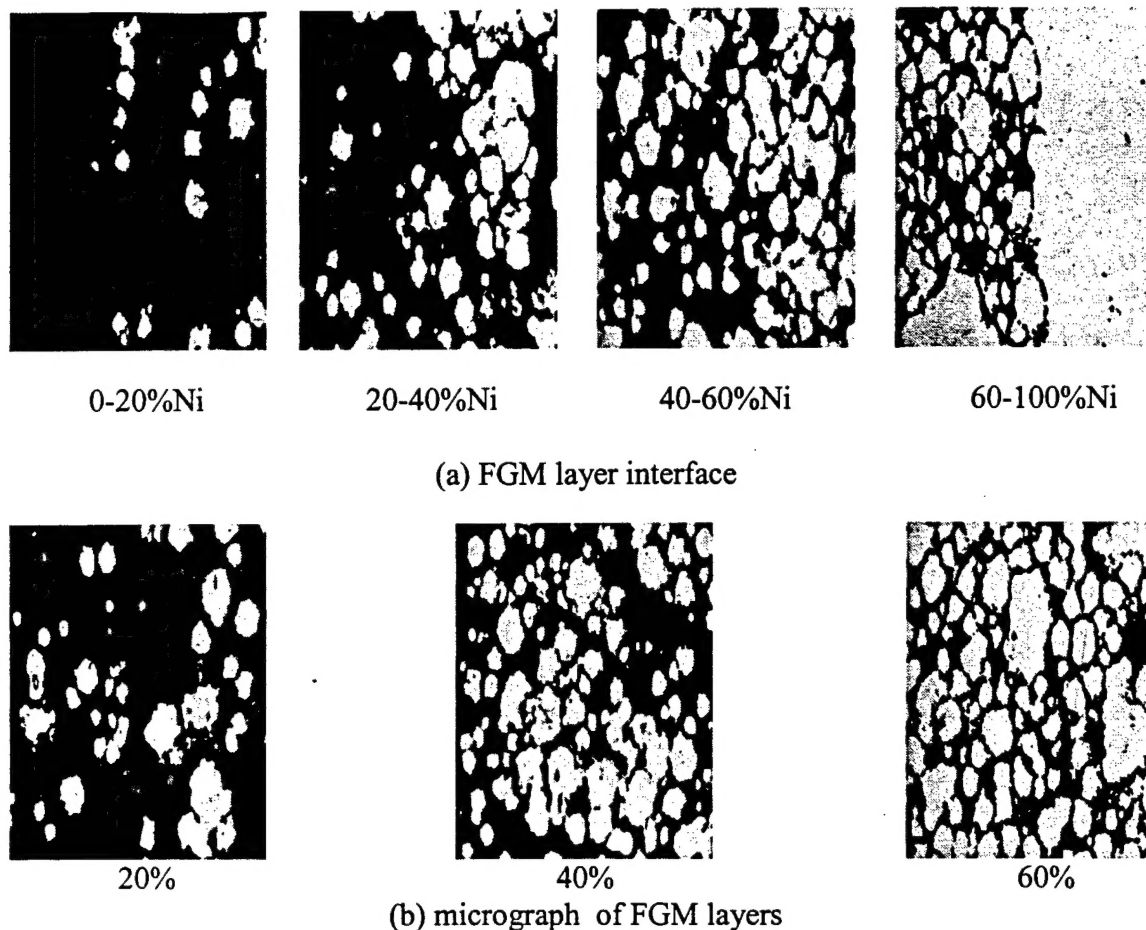
5

| 0-20%Ni | 20-40%Ni | 40-60%Ni | 60-100%Ni |

(a) FGM layer interface

| 20% | 40% | 60% |

(b) micrograph of FGM layers

Figure 4 Optical micrograph of metal /ceramic Ni/ZrO$_2$ with 3.6 μm Ni, 0.2 μm ZrO$_2$ system FGM layers (a) FGM layer interface, (b) micrograph of FGM layers

For the Ni/ZrO$_2$ FGM system with small ZrO$_2$ particles of 0.2μm average diameter shown in Figure 4, the interface between the layers were strong and no cracks or deponding were found. The use of small ZrO$_2$ particles controlled the diffusion of the Ni phase as shown in Figure 4(b), where the Ni phase is homogenous though the composite.

Another FGM system was processed by Prof. Watanabe group, Tohuko University, Japan. The FGM system processed was SS/ZrO$_2$ that was processed by die compaction. The microstructure of the SS/ZrO$_2$ was obtained as shown in Figure 5, showing the FGM interface as well as the FGM layers. The graph also shows a three-dimensional view of the 30%SS layer which is of particular interest to us as will be explained later.
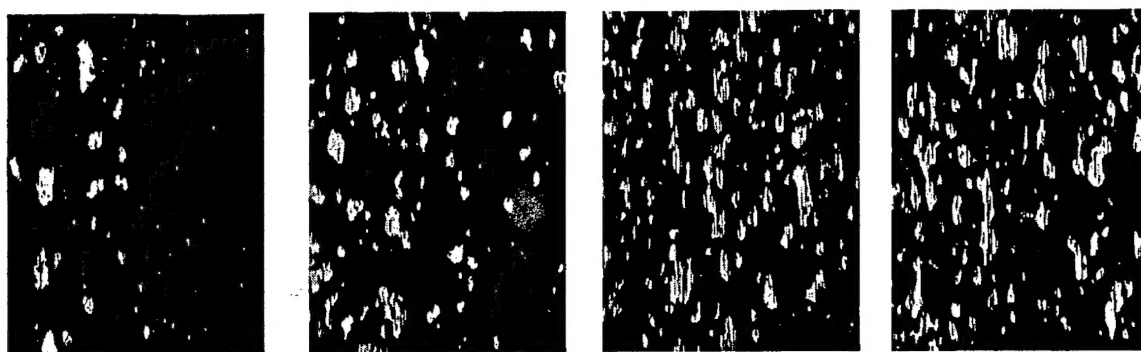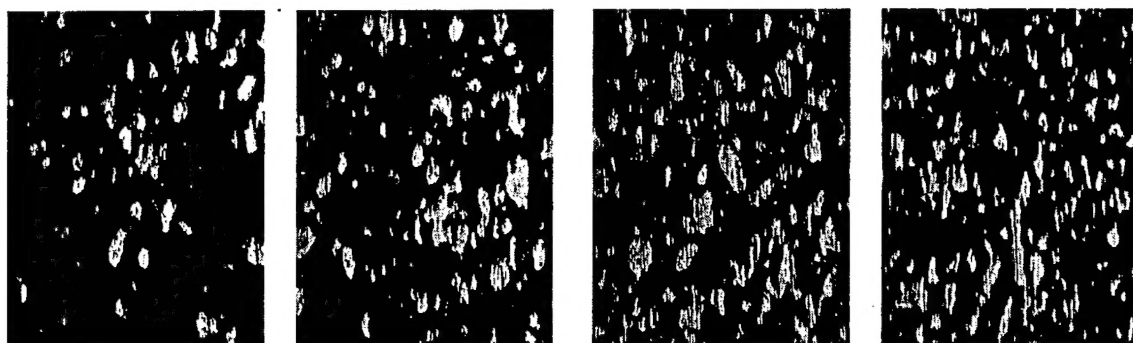
0-10% SS　　　10-20% SS　　　20-30% SS　　　30-40% SS

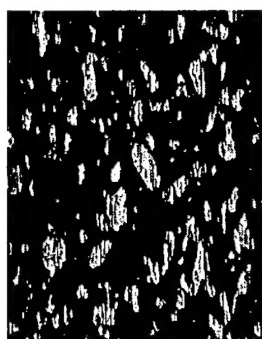(a) FGM layer interface

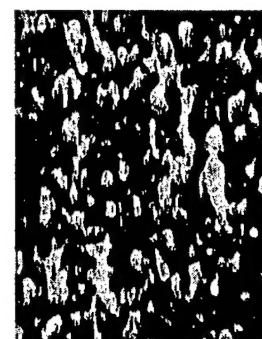10% SS　　　　20% SS　　　　30% SS　　　　40% SS

(b) micrograph of FGM layers

x-plane　　　　　　　y-plane　　　　　　　z-plane

(c) sectional view of 30%SS

Figure 5 Optical micrograph of metal /ceramic SS/ZrO$_2$ FGM layers
(a) layer interface ,(b) FGM layer of each layer (c) 3-D micrograph of 30%SS layer

2. Characterization Of FGM Microstructure And Mechanical Properties (Modulus And Fracture Resistance)

2.1 Experimental results

The FGM system was characterized for structural applications. The stiffness of the material was investigated experimentally as well as analytically. The experimental tests were done on SS/ZrO$_2$ specimen using compression testing by precisely cutting one layer and applying compression load to establish the modulus at each layer of a given FGM specimen. The analytical part was done through average mean theory of Eshilby's inhomogeneous inclusion method (Eshelby, 1957). Figure 6(a) shows the Young's
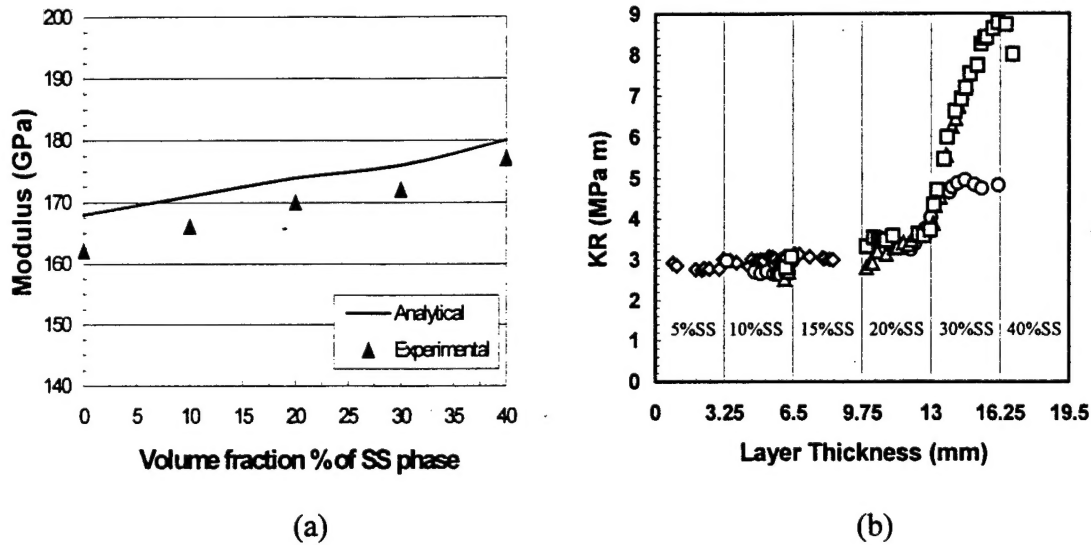
Figure 6 Mechanical properties of SS/ZrO$_2$ FGM,
(a) Young's modulus, (b) fracture resistance K_R

modulus of SS/ZrO$_2$ of each layer of the material along the FGM layer thichness, indicating a good agreement between the experiment and the prediction by Eshelby's model (Taya and Arsenault, 1989). The fracture resistance tests were conducted using a chevron-notched, wedge-loaded, double cantilever beam (WL-DCB) specimen. The details of WL-DCB specimen is given elsewhere (Li et. al., 1995). The moiré interferometry grating consisting of aluminum-epoxy was attached in the front of the specimen to determine the displacement along the y- axis, u_y. The displacement, u_y, along with the applied load were input into finite element program, ABAQUS. Then the fracture resistance, K_R is computed from the FEM results. The experimental data of the fracture resistance (K_R) versus crack length (Δa) of the SS/ZrO$_2$ FGM specimens plotted in Figure 6(b) indicates that the K$_R$ increases gradually with the increase in the volume fraction of stainless steel (SS) and then exhibits a sharper increase at and around the interface between 80%PSZ/20%SS and 70%PSZ/30%SS FGM layers. A study on the microstructure revealed that the sharp increase of the fracture resistance nearly coincides with the onset of SS phase percolation network. In Figure 5(c) SS phase is isolated at lower volume fraction of SS, and then it starts forming a percolation network at some f (close to 30%), then as much higher $f's$, ZrO$_2$ phase becomes isolated. The threshold of

8

percolation exists around the 30%SS volume fraction. Figure 7 shows one example of such a percolation path at the 30%SS region. The percolation path appears to exist more likely along the z-axis only as compared to the x-y plane as shown in figure 5(c).
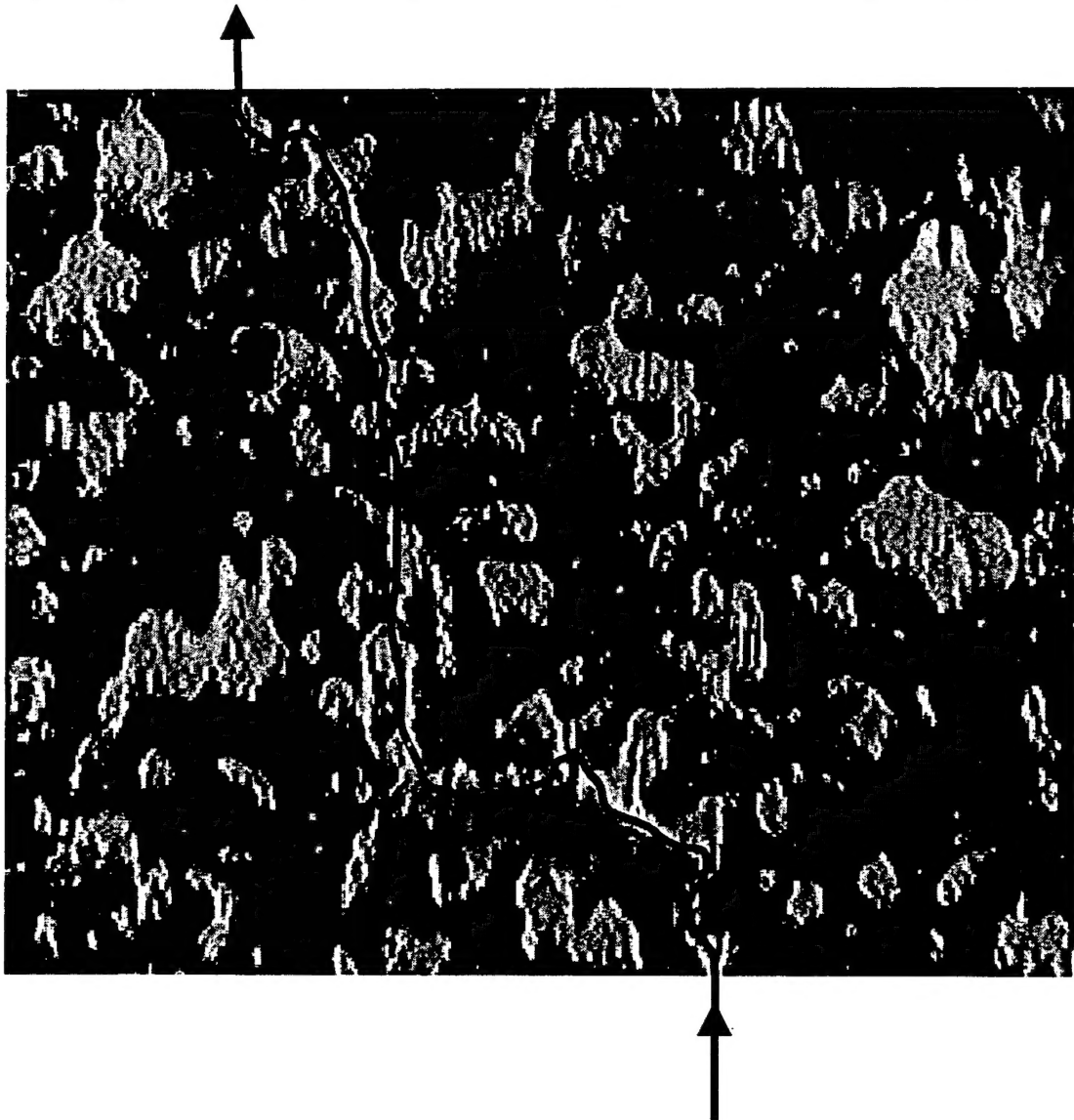

Figure 7 percolation path through 30%SS in the z-plane

For further investigation, Ni/ZrO$_2$ systems of two different ZrO$_2$ particle sizes were fabricated. For each system, percolation network of metal phase appears to start forming at around 30%or so. Since microscope was not a perfect tool to measure a percolation network, electrical resistively measurement used to verify the existence of the percolation network. The percolation threshold was studied experimentally by measuring the resistively of each layer. Figure 8(a) represent the resistively analysis of the two different Ni/ZrO$_2$ systems. It is found in Figure 8(a) that the electrical resistivity jumps around 20% for the 3.6 μm Ni, 25 μm ZrO$_2$ FGM system, while about 40% for the 3.6 μm Ni, 0.2 μm ZrO$_2$ FGM system. Figure 8(b) represents the electrical resistivity of SS/ZrO$_2$ FGM system and the percolation threshold is found to be around 30%.
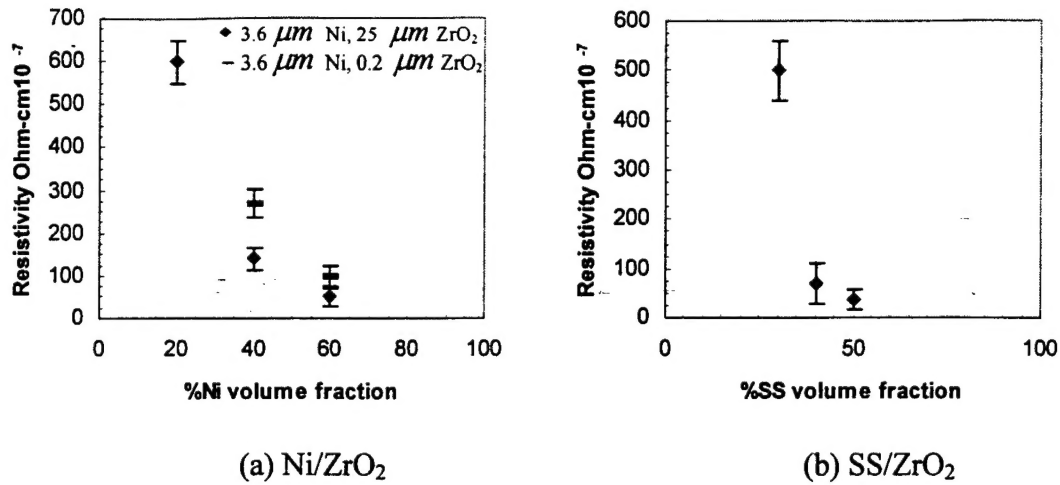
(a) Ni/ZrO$_2$ (b) SS/ZrO$_2$

Figure 8 Percolation threshold of (a) Ni/ZrO$_2$ and (b) SS/ZrO$_2$

The fracture resistance of the Ni/ZrO$_2$ materials was analyzed by using the WL-DCB specimen and the results of K_R versus volume fraction of the metal phase are shown in Figure 9. The system with smaller particle size of ZrO$_2$ has higher fracture toughness. The use of large ZrO$_2$ particles caused the Ni particles to agglomerate and to create islands of Nickel as shown in Figure 3. For example, comparing the Ni/ZrO$_2$ FGM micrographs of 60%Ni phase, Figure 3(b) for small sized ZrO$_2$ particles and Figure 4(b) for large sized ZrO$_2$ particles, one can notice that the distribution of the Ni phase (white color in the figures) with the small sized ZrO$_2$ is more homogeneous than that of the large sized ZrO$_2$, thus more effective in arresting the advancing crack in the ZrO$_2$ ceramic phase. This explains why the FGM with small ZrO$_2$ has higher fracture resistance (K_R) than that with larger ZrO$_2$.
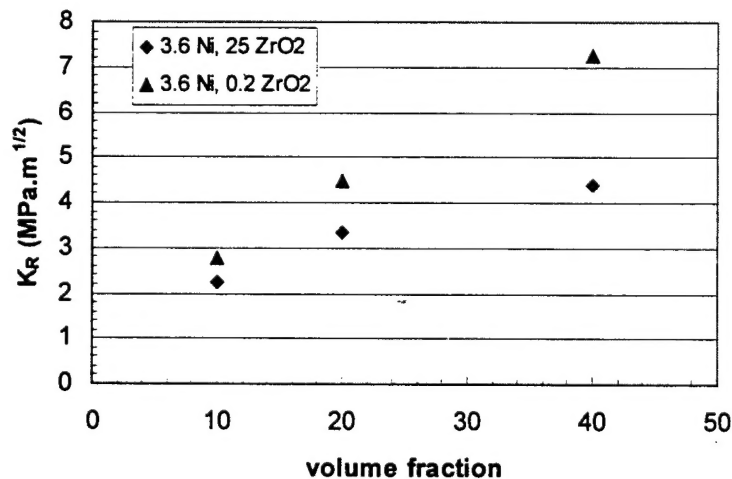

Figure 9 Fracture resistance, K_R of Ni/ZrO$_2$

2.2   Discussion

The toughening mechanism of the SS/ZrO$_2$ FGM is investigated. Two possible mechanisms studied, toughening through residual stress and through percolation.

Toughening through residual stresses

The grain sizes of the filler particles, stainless steel, were measured, then the toughening model on the residual stress in the metal phase due to the coefficient of thermal expansion (CTE) mismatch was used. The coefficient of thermal expansion mismatch between ceramic and metal phases is expected to induce the (internal) residual stress field after the FGM is cooled down from the processing temperature, resulting in the average compressive stress in the ceramic phase. This compressive residual stress in the ceramic phase plays a key role in crack closure in the ceramic phase. Taya $et.$ $al.$ proposed the toughening of a ceramic material by this model (Taya $et.$ $al.$, 1989).

The average residual stress in the ceramic phase, σ_c , and the increase in fracture resistance, ΔK_R are given by

$$\sigma_c = \frac{2E_{PSZ}f_{SS}\beta}{(1-f_{SS})(\beta+2)(1+v_{PSZ})+3\beta f_{SS}(1-v_{PSZ})} \times \int_{T_{PROCESS}}^{T_{TEST}}(\alpha_{SS}-\alpha_{PSZ})dT \qquad (1)$$

$$\Delta K_R = 2\sigma_c\sqrt{\frac{2\overline{d}(1.085/\sqrt{f_{SS}}-1)}{\pi}} \qquad (2)$$

Then, the increase in the fracture resistance in the ceramic phase, ΔK_R of the SS/ZrO$_2$ FGM layers with ceramic rich (i. e. volume fraction of SS being 0-25%), Figure 6(b), can be explained by this thermal residual stress model. However, the jump in K_R value around 30%SS phase can not. Hence, we attempt to explain this jump in K_R in view of percolation phenomenon.

The materials properties for stainless steel (SS) and zirconia (ZrO2) are given below and the increase in fracture toughness in Table 3

$$E_{PSZ} = 168.8GPa \qquad E_{SS} = 196.0GPa$$
$$v_{PSZ} = 0.3 \qquad v_{SS} = 0.26$$
$$\alpha_{PSZ} = 11.1 \times 10^{-6}/°C \qquad \alpha_{SS} = 14.0 \times 10^{-6}/°C$$

Stainless Steel Volume fraction f_{SS}	Average Particles size, $\overline{d}$, mm	Average thermal stress σ_c, MPa (in compression)	The increase in fracture toughness, ΔK_R, MPa
0.1	9.607	41.12	0.317
0.2	11.393	85.76	0.55
0.3	11.563	134.4	0.722
0.4	11.739	187.6	0.867

Table 3 Average thermal stress σ_c and the increase in fracture toughness ΔK_R

11

Toughening through percolation

Percolation of SS particles in the SS/ZrO$_2$ system can be explained by the following equations

$$\left(K_R\right)_{com} = \left(K_R\right)_{ss}\left(f - f^*\right)^t \qquad \text{for} \quad f \geq f^*$$

$$\left(K_R\right)_{com} = \left(K_R\right)_{psz}\left(f^* - f\right)^{-s} \qquad \text{for} \quad f < f^* \qquad\qquad (3)$$

$$\left(K_R\right)_{com} = \left(\left(K_R\right)_{psz}\right)^{u}\left(\left(K_R\right)_{ss}\right)^{1-u} \qquad \text{for} \quad f \cong f^*$$

where

$$u = \frac{t}{t + s}$$

where $\left(K_R\right)_{com}, \left(K_R\right)_{psz}$, and $\left(K_R\right)_{ss}$ are the fracture resistance of composite, zirconia and stainless steel, respectively. f is the volume fraction of the SS phase while f^* is the threshold volume fraction of the SS phase. From Figure 6(b), s, t, and u are obtained as in Table 4 by knowing K_R and volume fraction, f,

f	$(K_R)_{com}$	
0.31	10	$t = 0.02288$
0.29	4	$s = 0.0625$
0.3	7.82	$u = 0.268$

Table 4 s, t, and u parameter at the percolation threshold of SS/ZrO$_2$ system

The toughening profile of SS/ZrO$_2$ system based on the percolation power law type is shown in Figure 10
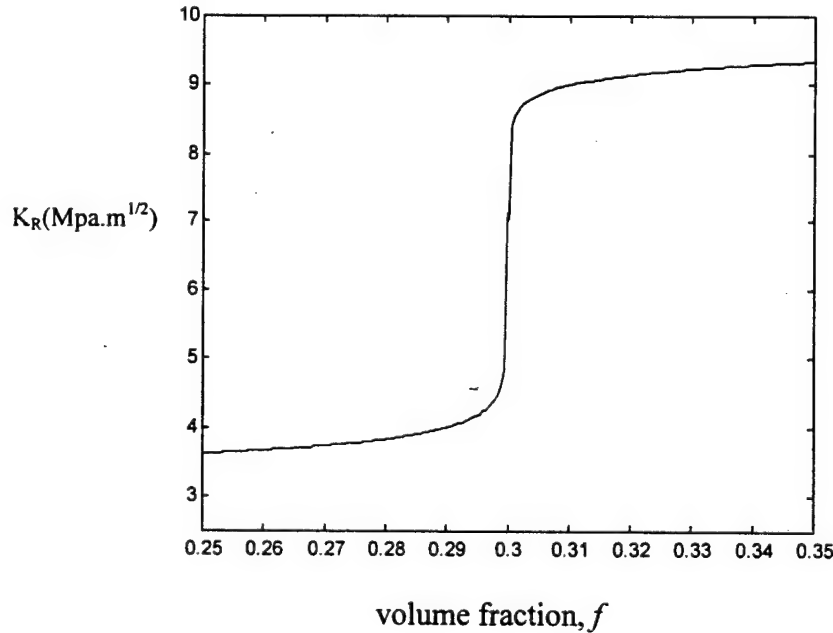

Figure 10 K_R of SS/ZrO$_2$ system predicted by the percolation power law

The exponent t in eq. (3) for $f \geq f^*$ estimated as $t = 0.02288$, which seems to be a bit lower than that found in the percolation in the electrical resistivity of conductor-insulator mixture. It should be pointed out here that the exponent t for the mechanical percolation is quite different from that in the electrical percolation.

3. Modeling Of A Piezoelectric FGM Plate

Analytical study on piezoelectric laminate with functionally graded microstructure (FGM) was established to construct a hierarchical modeling (Almajid et. al. (2000)). The study consist of two models, one at microscopic level focusing on the microstructure of each FGM layer, the other on laminating FGM layers to predict the out-of-plane displacement of the FGM plate under applied electric field. The standard piezoelectric actuator plate is of bimorph type. These kinds of actuators develop high stresses in the interface between the materials as shown in Figure 11. An FGM model has been investigated to reduce the otherwise high stresses. FGM have shown a remarkable reduction of the residual stresses.
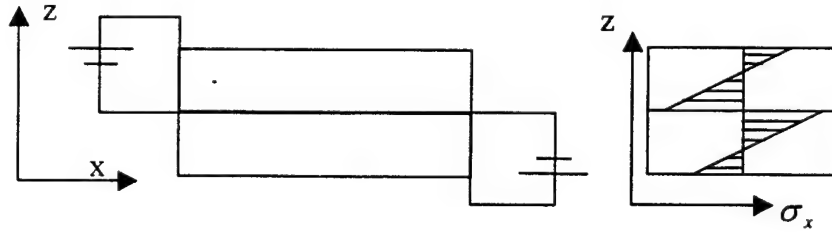

Figure 11 Typical stresses generated in a bimorph piezo-actuator

Figure 12 shows typical FGM structure where the mechanical and physical properties vary along the z-direction.
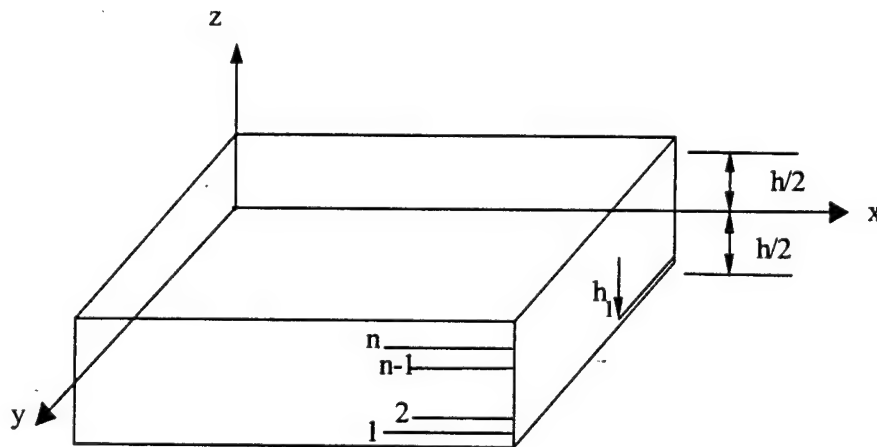

Figure 12 Piezoelectric FGM plate

A piezoelectric laminate consists of n laminae, each being a piezoelectric material with specified electroelastic properties. The constitutive equations of a piezoelectric material in the absence of temperature effects are given by

$$\sigma_{ij} = C_{ijkl}\varepsilon_{kl} - e_{mij}E_m \tag{4}$$

13

where $\sigma_{ij}, \varepsilon_{ij}$ are the stress and strain tensor components respectively, E_m is the electric field vector component, C_{ijkl} is the elastic stiffness tensor, and e_{mij} are the piezoelectric coefficients. The electroelastic constants of each lamina may be computed from some micromechanical model such as the Eshelby type method as outlined by Dunn and Taya (1993a, b). Two analytical modeling has been established to predict the out-of-plane displacement and stress field of laminated piezoelectric plate, Classical Lamination Theory (CLT) and 2D-elasticity solution.

3.1 Classical Lamination Theory (CLT)

Classical lamination theory (CLT), as found in any composite textbook such as Gibson(1994) assumes a state of plane stress along the z-axis where, $\sigma_z = \sigma_{xz} = \sigma_{yz} = 0$. The constitutive equations of a piezoelectric lamina, eq. 4, under applied electric field in the z direction only, and under the assumption of plane stress along the z-axis, reduces to

$$\begin{Bmatrix} \sigma_x \\ \sigma_y \\ \sigma_{xy} \end{Bmatrix} = \begin{bmatrix} \overline{Q}_{11} & \overline{Q}_{12} & 0 \\ \overline{Q}_{21} & \overline{Q}_{22} & 0 \\ 0 & 0 & Q_{66} \end{bmatrix}_i \begin{Bmatrix} \varepsilon_x^0 + z\kappa_x \\ \varepsilon_y^0 + z\kappa_y \\ \gamma_{xy}^0 + z\kappa_{xy} \end{Bmatrix} - \begin{bmatrix} 0 & 0 & \overline{e}_{31} \\ 0 & 0 & \overline{e}_{32} \\ 0 & 0 & 0 \end{bmatrix} \begin{Bmatrix} 0 \\ 0 \\ E_z \end{Bmatrix} \tag{5}$$

where

$$\overline{Q}_{ij} = C_{ij} - \frac{C_{i3}}{C_{33}} C_{j3} \tag{6}$$

$$\overline{e}_{ij} = \frac{C_{i3}}{C_{33}} e_{33} - e_{ij}$$

It is noted here that $\overline{Q}_{ij}$, $\overline{e}_{ij}$ are the reduced stiffness constants and reduced piezoelectric constants that are modified by the assumption of plane stress and where $\varepsilon_x^0, \varepsilon_y^0$, and ε_{xy}^0 are the in-plane strain components at mid-plane, z=0 as shown in Fig. 11, κ_x, κ_y, and κ_{xy} are the curvatures of the plate.

The resultant in-plane forces and bending moments are defined by

$$\{N, M\} = \sum_{i=1}^n \int_{h_{i-1}}^{h_i} \{\sigma\}(dz, zdz) \tag{7}$$

carrying out the integration through the plate thickness of h, the resultant forces and bending moments can then be written as

$$\begin{bmatrix} N \\ M \end{bmatrix} = \begin{bmatrix} A & B \\ B & D \end{bmatrix} \begin{Bmatrix} \varepsilon^0 \\ \kappa \end{Bmatrix} - \begin{bmatrix} N^E \\ M^E \end{bmatrix} \tag{8}$$

where

$$[A, B, D] = \sum_{i=1}^n \int_{h_{i-1}}^h [\overline{Q}](dz, zdz, z^2 dz) \tag{9a}$$

$$[N, M]^E = \sum_{i=1}^n \int_{h_{i-1}}^{h_i} [\overline{e}] \{E\}(dz, zdz) \tag{9b}$$

14

where h_{i-1} and h_i are the distance from the bottom of the plate to the bottom and top interfaces of the ith lamina respectively, with $i = 1,2, \dots n$. Hence the thickness of the ith lamina is then h_i-h_{i-1}. Under the applied electric field or temperature change only, i.e. M=N=0 in eq. (8), the in-plane strain and curvature can be solved as

$$\begin{bmatrix} \varepsilon^o \\ \kappa \end{bmatrix} = \begin{bmatrix} a & b \\ b & d \end{bmatrix} \begin{bmatrix} N^E \\ M^E \end{bmatrix} \tag{10}$$

where

$$\begin{bmatrix} a & b \\ b & d \end{bmatrix} = \begin{bmatrix} A & B \\ B & D \end{bmatrix}^{-1}$$

Under a given electric field throughout the laminate, one can then predict the stress and displacement field of each layer as well as the out-of-plane displacement of the composite plate.

Different types of FGM were studied as shown in the Figure 13 where the conventional bimorph type, one-sided FGM, and FGM bimorph are shown.

(a) bimorph   (b) one sided FGM laminate   (c) FGM bimorph
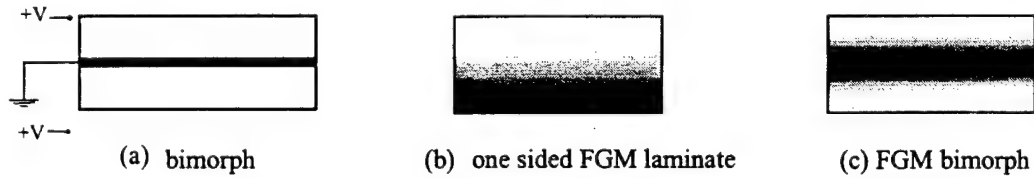
Figure 13 Different types of FGM

The distribution of mechanical and piezoelectric (PZT) properties varies throughout the FGM as shown in Figure 14.
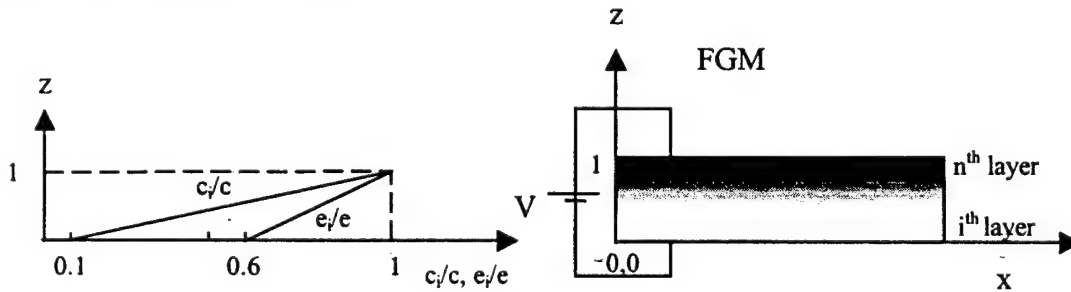

Figure 14 The distribution of mechanical and piezoelectric properties in the FGM

The distribution of both mechanical and piezoelectric properties could be explained through the following formula

$$C_i = [0.1 + 0.225(i-1)]C_{PZT}$$

$$e_i = [0.6 + 0.1(i-1)]e_{PZT}$$

$$i = 1,2,\dots..$$

where C_i, e_i are the mechanical and piezoelectric properties of the i-th layer, respectively. C_{PZT}, e_{PZT} are the mechanical and piezoelectric properties of the piezoelectric material. The mechanical and piezoelectric profile of the FGM bimorph is shown in Figure 15. The properties are increasing toward the middle as FGM-bimorph type A while they are decreasing in FGM-bimorph type B.
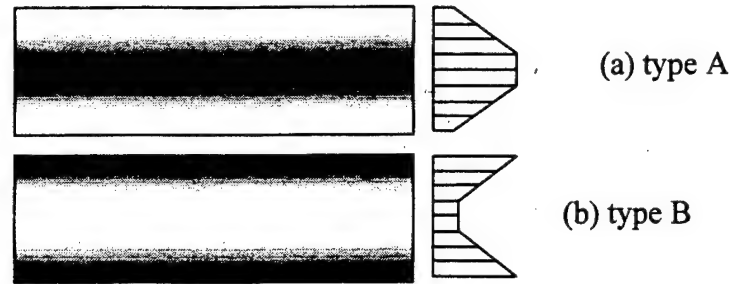

(a) type A

(b) type B

Figure 15 FGM-bimorph profile

The mechanical and piezoelectric properties of the piezoelectric and the mid-plane gold layer are shown in Table 5.

	C_{11} (GPa)	C_{12} (GPa)	C_{13} (GPa)	C_{33} (GPa)	C_{44} (GPa)	e_{31} (C/m^2)	e_{33} (C/m^2)	e_{15} (C/m^2)
PZT	121	75.4	75.2	111	21.1	-5.4	15.8	12.3
Au	101.43	41.63	41.63	101.43	29.9	0	0	0

Table 5 mechanical and piezoelectric properties

The out of plane displacement of each case were calculated and tabulated in Table 6.

Type of FGM microstructure	Standard bimorph, Fig. 2(a)	FGM one-sided, Fig. 2(b)	Bimorph FGM, Fig. 4(a) Type A	Bimorph FGM, Fig. 4(b) Type B
Electric Field (V/mm)	1,000	1,000	1,000	1,000
Applied Voltage (V)	208	500	208	208
Laminate thickness (mm)	0.5	0.5	0.5	0.5
No. of layers	2	5	10	10
Layer thickness(mm)	0.208 Au = 0.082	0.1	0.0416 Au = 0.082	0.0416 Au = 0.082
Curvature (1/m)	0.99	0.992	2.15	0.773
Max. σ_x (MPa)	12.18	8.5	9.8	9.36
Out-of –plane displacement (mm) for plate length of 50mm	0.618	0.62	1.34	0.48

Table 6 Comparison of out-of-plane displacement and maximum in-plane stress for various types of piezo-composite plates

The FGM bimorph with mid-plane layer exhibited the maximum out of plane displacement. The results of the in-plane stresses between layers of each case have been are shown in Figure 16.

(a) FGM bimorph type B

(b) FGM bimorph type A
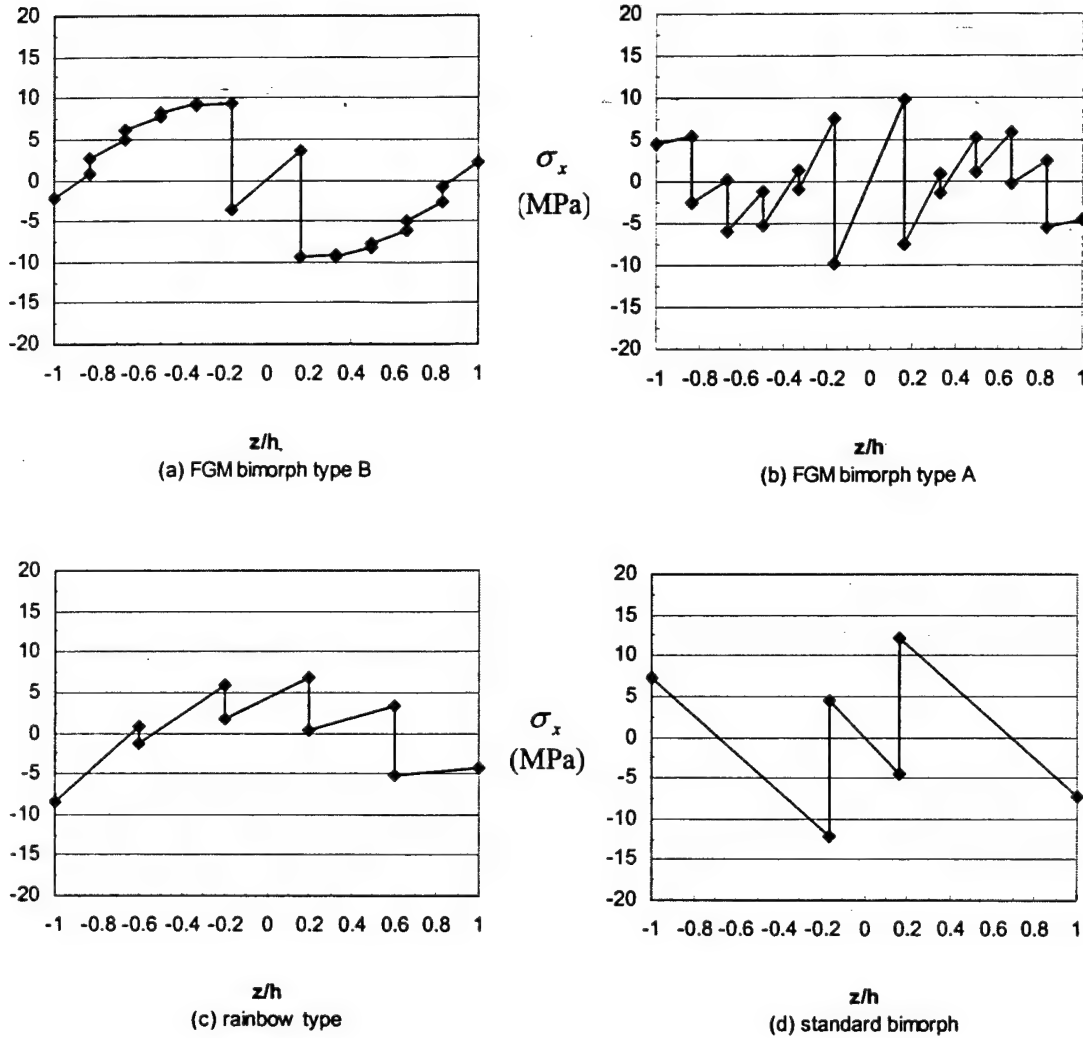
(c) rainbow type

(d) standard bimorph

Figure 16 in-plane stresses throughout
the plate thickness (z/h)

As it can be seen from the graph, there exist high in-plane stresses between the layers. That stress reached high in the case of bimorph. The high residual stresses have been reduced through the use of FGM especially the FGM bimorph with intermediate layer. The gold layer serves as relaxation for the piezoelectric since it does not posses piezoelectric properties. There is a need to investigate on the shear stresses associated with the in-plane stresses by using a more accurate model such as FEM.

3.2   2D elasticity model for piezo composite laminates in cylindrical bending
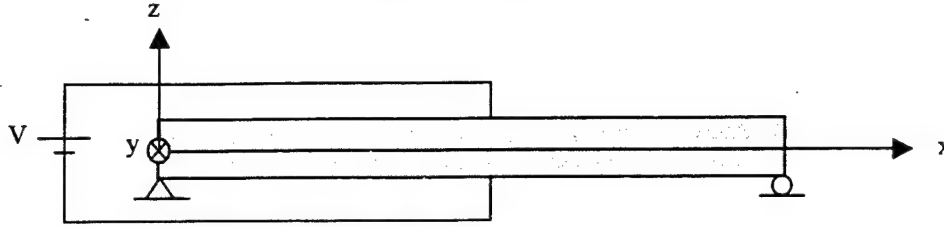

Figure 17 Simply supported piezoelectric plate under a state
of plane strain in the y-direction

For a laminate of multi orthotropic layers of piezoelectric material, the cylindrical bending was constructed by following the solution method developed by Pagano (1969) and using the condition of plane strain along the y-direction where, $\varepsilon_y = \varepsilon_{xy} = \varepsilon_{yz} = 0$ as shown in Figure 17. The laminate is simply supported on the ends. The constitutive equations of a piezoelectric material in absence of temperature are given by

$$\varepsilon_{ij} = S_{ijkl}\sigma_{kl} + d_{mij}E_m$$
(11)

where $\sigma_{ij}, \varepsilon_{ij}$ are stress and strain tensor components, E_m is electric field vector component, S_{ijkl} are elastic compliance, d_{mij} are the piezoelectric coefficients. The reduced constitutive equations for plane strain is given as,

$$\begin{Bmatrix} \varepsilon_x \\ \varepsilon_z \\ 2\varepsilon_{xz} \end{Bmatrix} = \begin{bmatrix} R_{11} & R_{13} & 0 \\ R_{13} & R_{33} & 0 \\ 0 & 0 & R_{55} \end{bmatrix} \begin{Bmatrix} \sigma_x \\ \sigma_z \\ \sigma_{xz} \end{Bmatrix} + \begin{bmatrix} 0 & 0 & \bar{d}_{31} \\ 0 & 0 & \bar{d}_{33} \\ d_{15} & 0 & 0 \end{bmatrix} \begin{Bmatrix} E_x \\ E_y \\ E_z \end{Bmatrix}$$
(12)

where R_{ij} and $\bar{d}_{ij}$ are the reduced compliance and piezoelectric coefficient and are defined as

$$R_{ij} = S_{ij} - \frac{S_{i3}}{S_{33}}S_{j3}$$

$$\bar{d}_{ij} = d_{ij} - \frac{S_{i3}}{S_{33}}d_{3j}$$
(13)

where S_{il} and d_{ij} are the compressed forms of S_{ijkl} and d_{mij}.

The boundary conditions of the simply supported piezoelectric laminate are given by

$$\sigma_x(x=0,z) = \sigma_x(x=l,z) = 0$$

$$w(x=0,z) = w(x=l,z) = 0$$
(14)

while the prescribed surface traction-free conditions of the upper and lower surfaces of the laminate require

$$\sigma_z\left(x,-\frac{h}{2}\right) = \sigma_z\left(x,\frac{h}{2}\right) = 0$$

$$\sigma_{xz}\left(x,-\frac{h}{2}\right) = \sigma_{xz}\left(x,\frac{h}{2}\right) = 0$$
(15)

The interface continuity conditions at each layer are given by

$$\sigma_z^i\left(x,\frac{h_i}{2}\right) = \sigma_z^{i+1}\left(x,\frac{h_i}{2}\right)$$

$$\sigma_{xz}^i\left(x,\frac{h_i}{2}\right) = \sigma_{xz}^{i+1}\left(x,\frac{h_i}{2}\right)$$

$$u_i\left(x,\frac{h_i}{2}\right) = u_{i+1}\left(x,\frac{h_i}{2}\right) \qquad (i = 1,2, \ldots. N\text{-}1) \qquad (16)$$

$$w_i\left(x,\frac{h_i}{2}\right) = w_{i+1}\left(x,\frac{h_i}{2}\right)$$

where i represent the interface ID number between the ith and the $(i+1)^{th}$ laminae with $i = 1 \sim N\text{-}1$ and the topmost and bottommost interfaces are defined as 1st and $(N\text{-}1)^{th}$ interfaces, respectively, while h_i represent the thickness of the ith laminae. The top layer corresponds to $i = 1$ while the bottom layer is $i=N$. The electric field is applied in the z-direction through the thickness of the laminate. The electric field is expressed in the form of Fourier series as

$$E_z = E_o \sum_{n=1,3,5,..}^{\infty} \frac{4}{n\pi} \sin(\lambda x) \qquad (17)$$

$$E_x = E_y = 0$$

where $\lambda = \dfrac{n\pi}{l}$, and for higher values of n, a nearly constant electric field can be realized.

Following Pagano (1969), the stress field in the ith layer is assumed to be

$$\sigma_x^i = f_i''(z)\sum_n^{\infty} \frac{4}{n\pi}\sin\left(\frac{n\pi}{l}x\right)$$

$$\sigma_z^i = -f_i(z)\sum_n^{\infty} \left(\frac{n\pi}{l}\right)^2 \frac{4}{n\pi}\sin\left(\frac{n\pi}{l}x\right) \qquad (18)$$

$$\sigma_{xz}^i = -f_i'(z)\sum_n^{\infty} \left(\frac{n\pi}{l}\right)\frac{4}{n\pi}\cos\left(\frac{n\pi}{l}x\right)$$

where $f_i(z)$ is an unknown function to be determined. The equilibrium equations given by

$$\sigma_{ij,j} = 0 \qquad (19)$$

are automatically satisfied if eq.(18) is substituted into eq.(19). The 2D-strain compatibility equation is given by

$$2\varepsilon_{xz,xz} - \varepsilon_{z,xx} - \varepsilon_{x,zz} = 0 \qquad (20)$$

Substitution of eq.(12) into eq.(20) and use of eqs.(17) and (18) leads to a fourth order ordinary differential equation

$$R_{11}^i f_i''''(z) - \lambda^2\left(2R_{13}^i + R_{55}^i\right)f_i''(z) + \lambda^4 R_{33}^i f_i(z) = \lambda^2 \overline{d}_{33} E_o \qquad (21)$$

19

The solutions $f_i(z)$ can be expressed by

$$f_i(z) = \sum_{j=1}^{4} A_{ji} \exp(m_{ji} z_i) + \frac{(\overline{d}_{33})^i E_o}{\lambda^2 R_{33}^i} \tag{22}$$

where A_{ji} are constant and the values of m_{ji} are given by

$$\binom{m_{1i}}{m_{2i}} = \pm \lambda \left(\frac{a_i + b_i}{c_i} \right)^{\frac{1}{2}}$$

$$\binom{m_{3i}}{m_{4i}} = \pm \lambda \left(\frac{a_i - b_i}{c_i} \right)^{\frac{1}{2}} \tag{23}$$

where

$$a_i = R_{55}^i + 2R_{13}^i$$

$$b_i = \left[a_i^2 - 4R_{11}^i R_{33}^i \right]^{\frac{1}{2}} \tag{24}$$

$$c_i = 2R_{11}^i$$

The stress field solutions of the ith layer can be found using eq.(22) as

$$\sigma_x^i = \sum_{n=1,3,..}^{\infty} \sum_{j=1}^{4} A_{ji} m_{ji}^2 \exp(m_{ji} z_i) \frac{4}{\pi} \sin(\lambda x)$$

$$\sigma_z^i = \sum_{n}^{\infty} \left[\sum_{j=1}^{4} - A_{ji} \exp(m_{ji} z_i) \lambda^2 \frac{4}{\pi} \sin(\lambda x) - \frac{(\overline{d}_{33}) E_o}{R_{33}^i} \frac{4}{\pi} \sin(\lambda x) \right] \tag{25}$$

$$\sigma_{xz}^i = \sum_{n}^{\infty} \sum_{j=1}^{4} - A_{ji} m_{ji} \exp(m_{ji} z_i) \lambda \frac{4}{\pi} \cos(\lambda x)$$

while the displacement components are found from the strain-displacement relation,

$$u_i = \sum_{n}^{\infty} \left\{ \sum_{j=1}^{4} A_{ji} \exp(m_{ji} z_i) \left[\lambda R_{13}^i - \frac{R_{11}^i}{\lambda} m_{ji}^2 \right] + \left[\frac{R_{13}^i}{R_{33}^i} (\overline{d}_{33}) - (d_{31}) \right] \frac{E_o}{\lambda} \right\} \frac{4}{\pi} \cos(\lambda x)$$

$$w_i = \sum_{n}^{\infty} \sum_{j=1}^{4} A_{ji} \exp(m_{ji} z_i) \left[R_{13}^i m_{ji} - \frac{\lambda^2 R_{33}^i}{m_{ji}} \right] \frac{4}{\pi} \sin(\lambda x) \tag{26}$$

It is noted that the above solutions satisfy the boundary conditions of eq.(14) while the surface traction-free boundary conditions of eq.(15) and the interface continuity conditions of eq.(16), remain to be satisfied, resulting 4N equation for 4N unknown constants A_{ji}.

Figure 18 shows some of the results obtained by the 2D elasticity model and FEM, the distribution of the inter-laminar shear stress, τ_{xz} and normal stress, σ_x, near the free edge along the longitudinal (x axis) direction.
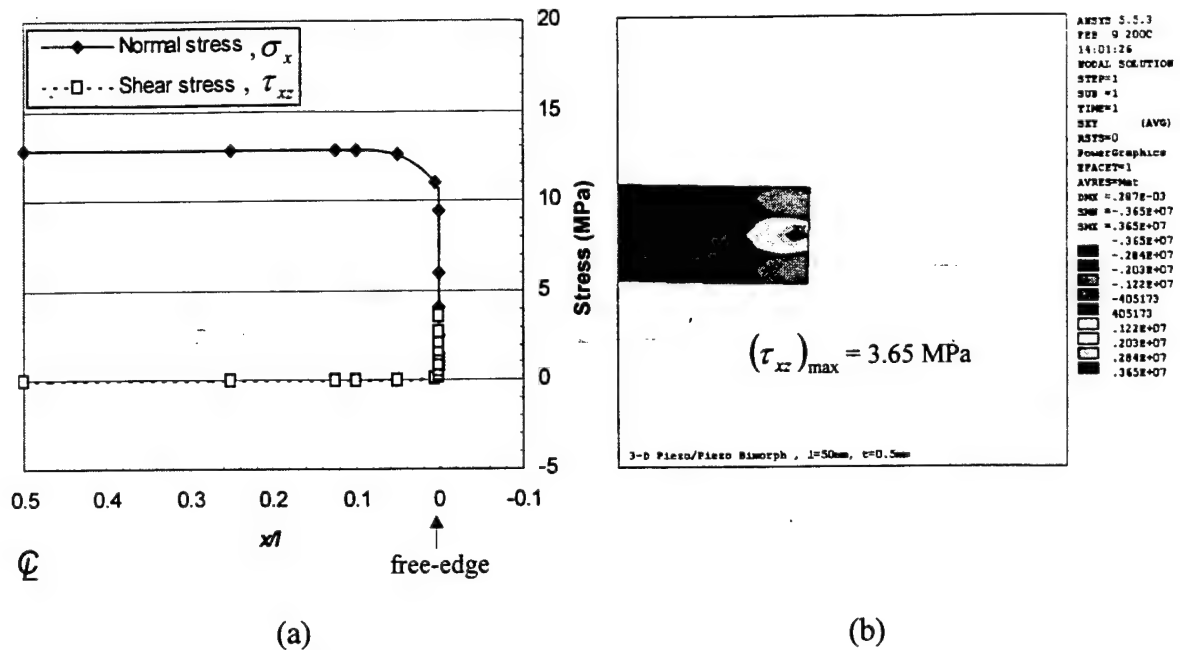
(a)   (b)

Figure 18 Distribution of normal stress, σ_x and inter-laminar shear stress, τ_{xz} near free edge of a standard bimorph piezo-actuator under applied voltage of 208V, predicted by (a) the 2D elasticity model and (b) FEM

It follows from Fig. 18 that the predicted interlaminar shear stress near the free edge by the 2D elasticity model is close to those by 2D FEM analysis.

4. Material Property Modeling For Fiber Based Piezoelectric FGM Bimorphs

Our work on piezoelectric FGM bimorphs has led to the need for accurate material properties for piezoelectric composites. One possible fabrication method for piezoelectric FGM actuators is through the use of stacked layers of piezo-ceramic fibers. In these devices the fiber volume fraction is graded from layer to layer thereby resulting in graded material properties, including piezoelectric coupling, from layer to layer. Due to the fact that the fiber diameter is nearly the same as the layer thickness within the composite and that within an FGM the fiber distribution is clearly not uniform through the thickness of the composite, a uniform packing of fibers in these devices is not achieved. Because of this deviation from idealized fiber packing many of the assumptions, including matrix connectivity, of most micromechanics models, including those based on Eshelby's (1957) work, are violated. This leads to the use of the finite element method (FEM) for evaluation of individual unit cells. Others have looked at this approach, but they assumed symmetries which are not actually present in reality.

4.1. The Fiber Based Piezoelectric FGM Bimorph

The basic design consists of stacking two piezoelectric FGM's into a symmetric bimorph as shown in Figure 19. The FGM laminates consist of piezoelectric ceramic fibers contained in an epoxy matrix. A second type of fiber, which is not piezoelectric, is used as a "place holder" in the layers with lower piezoelectric fiber volume fraction, v_f, to prevent adjacent layers from being pressed into each other during the cure cycle.
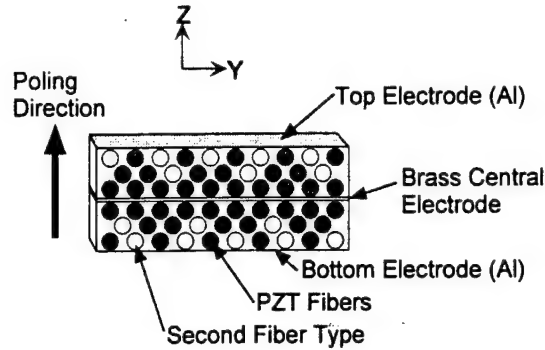
21

Figure 19. Schematic end view of the fiber based FGM bimorph actuator.

4.2. Modeling Fiber Based Piezoelectric Composite Material Properties

For the case of current piezoelectric fiber composites, the diameter of the fibers is almost as large as the layer thickness and simply examining v_f, does not give an accurate picture of the packing of the fibers. For this reason, the concept of ceramic line fractions in circular fiber composites was used. For this work the line fractions are labeled Y and Z, where Y is the ratio of fiber diameter to fiber centerline spacing within each layer, and Z is the ratio of fiber diameter to layer thickness.
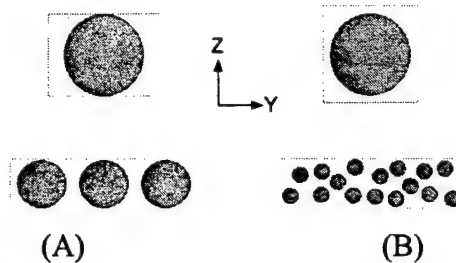

(A)   (B)

Figure 20. Rectangular versus square packing of circular fibers in a composite.
(A) Rectangular packing, top image showing $v_f = .56$, Z = .99 and Y = .71.
(B) Square packing, top image showing $v_f = .56$, Z = Y=.84.

This distinction between square and rectangular fiber packing is important as v_f in the FGM layers will be solely a function of Y, the in plane line fraction because all layers are the same thickness. Further, when considering that the dielectric constants of the fiber and the matrix differ by a factor of 100, examination of the top images in Figure 20 indicates that the electric field will be very different in the two different packing arrangements.

To show the deviation from the idealized results of most micromechanics models, it is useful to compare the FEM results to an analytical model. The recently published work of Mikata (2000) allows determination of the Eshelby tensor for a composite where the poling axis is perpendicular to the long axis of the fiber. Even with the limitations discussed above, use of Mikata's Eshelby tensor in the Mori-Tanaka (1973) mean field theory as outlined by Dunn and Taya (1993b) will provide a comparison to the FEM models to be used for material property determination.

The first step in the FEM analysis is to determine which unit cell to use and also which planes of symmetry may be used to minimize the computational effort required to solve the model. For this work the 1/2 symmetric unit cell was chosen as shown in Figure 21.
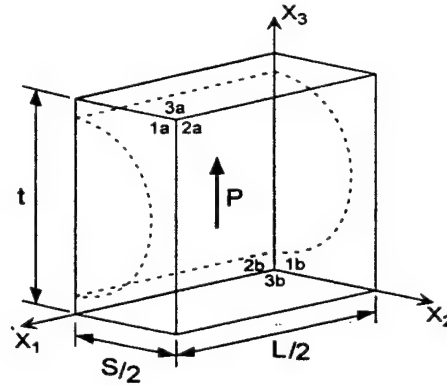
22

Figure 21. Schematic representation of 1/2 symmetric unit cell with faces labeled for boundary condition application. Poling axis is labeled as P in the figure. Faces 3a and 3b are the surface electrodes.

The choice to use the 1/2 symmetric unit cell which models the entire layer thickness was due to the fact that there is not a plane of electrical symmetry parallel to the 1-2 plane halfway between faces 3a and 3b. This electrical asymmetry is clearly seen from the plot of voltage versus thickness in a layer of the composite as shown in Figure 22.
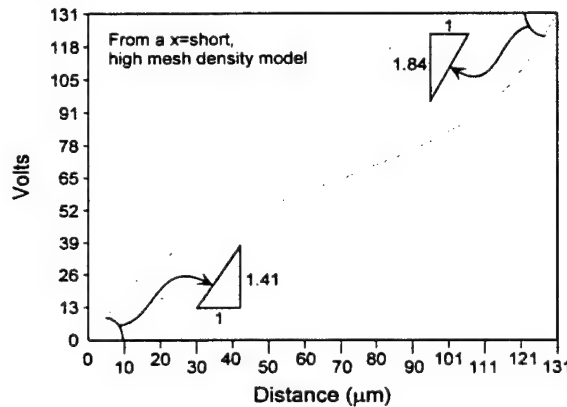

Figure 22. Plot of Voltage versus thickness.

The symmetry planes in this model are faces 1b and 2b or the 1-3 and 2-3 planes. These are clearly planes of mechanical and electrical symmetry. The boundary conditions for this unit cell are listed below in Table 7.

Face	Mechanical B.C.'s	Electrical B.C.'s
1a	All u_1 coupled	$D_1 = 0$
2a	All u_2 coupled	$D_2 = 0$
3a	All u_3 coupled	V coupled
1b	(Symm) $u_1 = 0$	$D_1 = 0$
2b	(Symm) $u_2 = 0$	$D_2 = 0$
3b	All u_3 coupled	V coupled

Table 7. Summary of boundary conditions on FEM 1/2 unit cell.

The model was meshed using 8-node hexahedral elements and a mapped mesh, as shown in Figure 23, as this would provide more accurate results than provided by a free mesh of

23

4-node tetrahedrons. The choice of the hexahedral elements would also allow easier control of mesh density in areas with high gradients such as the thin layer of matrix material between the fiber and the surface electrodes.
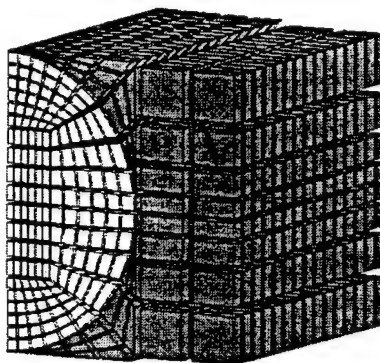

Figure 23. Exploded view of unit cell showing hexahedral elements. Fractions are Z = .99, Y = .56, v_f = .43. Shown in same orientation as unit cell of Figure 4.

The number of elements used in this work ranged from 3540 to 3660. The small range is due to the fact that most of the elements are in the region directly around the fiber and over the small range of Z line fractions considered, the shape of the elements is fairly constant. The solution at this element density was able to quickly converge and there are no poorly shaped elements. The larger number of elements was for the low Y line fraction. The small change added a few more elements in the area between fibers within each layer, although there was not too much concern in this area as the gradients were all fairly low. The practical upper limits of this model are Z = .995 and Y = .97 for v_f = .76, or very close to the maximum v_f of 0.785 for square packed cylindrical fibers.

The effective material properties were then found for a range of Y and Z line fractions by using the FEM method to run a series of hypothetical experiments based on those of Bent and Hagood (1997) with the addition of several new cases to determine the rest of the material properties. These experiments are summarized in Table 8 and the material properties for these calculations are listed in Table 9. It is further noted that in cases 5 through 7, some of the symmetry conditions listed in Table 7 were removed and replaced with a different set of constraints as the symmetric displacements would not always be valid in the shear cases.

Case	Mechanical Loading	Electrical Loading	Properties Obtained
1	$u_i = 0$ on faces 1a, 2a, 3a, 3b (zero strain)	Apply voltage V on top electrode, Ground bottom electrode	e_{31}, e_{32}, e_{33}, ε_{33}
2	Apply displacement u_1 on face 1a u_1 = free on 2a, 3a, 3b $u_2 = u_3 = 0$ on 1a, 2a, 3a, 3b	V = 0 on Electrodes (short circuit)	C_{11}, C_{12}, C_{13}, e_{31}
3	Apply displacement u_2 on face 2a u_2 = free on 1a, 3a, 3b $u_1 = u_3 = 0$ on 1a, 2a, 3a, 3b	V = 0 on Electrodes (short circuit)	C_{12}, C_{22}, C_{23}, e_{32}
4	Apply displacement u_3 on face 3a u_3 = free on 1a, 2a; $u_3 = 0$ on 3b $u_1 = u_2 = 0$ on 1a, 2a, 3a, 3b	V = 0 on Electrodes (short circuit)	C_{32}, C_{32}, C_{33}, e_{33}
5	Apply displacement u_2 on face 3a u_2 = free on 1a, 2a, 2b; $u_2 = 0$ on 3b $u_1 = u_3 = 0$ on 1a, 2a, 2b, 3a	V = 0 on Electrodes (short circuit)	C_{44}, e_{24}
6	Apply displacement u_3 on face 1a u_3 = free on 2a, 3a, 3b; $u_3 = 0$ on 1b $u_1 = u_2 = 0$ on 1a, 1b, 2a, 3a, 3b	V = 0 on Electrodes (short circuit)	C_{55}, e_{15}
7	Apply displacement u_1 on face 2a u_1 = free on 1a, 1b, 3a, 3b; $u_3 = 0$ on 2b $u_2 = u_3 = 0$ on 1a, 1b, 2a, 2b, 3a, 3b	V = 0 on Electrodes (short circuit)	C_{66}

Table 8. Load cases for FEM 1/2 symmetric unit cell.

	C_{11} (Gpa)	C_{12} (Gpa)	C_{13} (Gpa)	C_{33} (Gpa)	C_{44} (Gpa)	e_{31} (C/m^2)	e_{33} (C/m^2)	e_{15} (C/m^2)	$\varepsilon_{11}/\varepsilon_0$	$\varepsilon_{33}/\varepsilon_0$
PZT-5A	121	75.4	75.2	111	21.1	-5.4	15.8	12.3	916	830
Improved Epoxy	10.8	5.7	5.6	10.9	2.7	-0.002	0.007	0.005	7.3	7.3

Table 9. Material properties.

Some of the results of these analyses are plotted below in Figures 24 and 25 along with the results from the micromechanics model using Mikata's Eshelby Tensor as mentioned above. The dashed vertical line is $v_f = 0.785$, or the maximum square packing of round fibers.
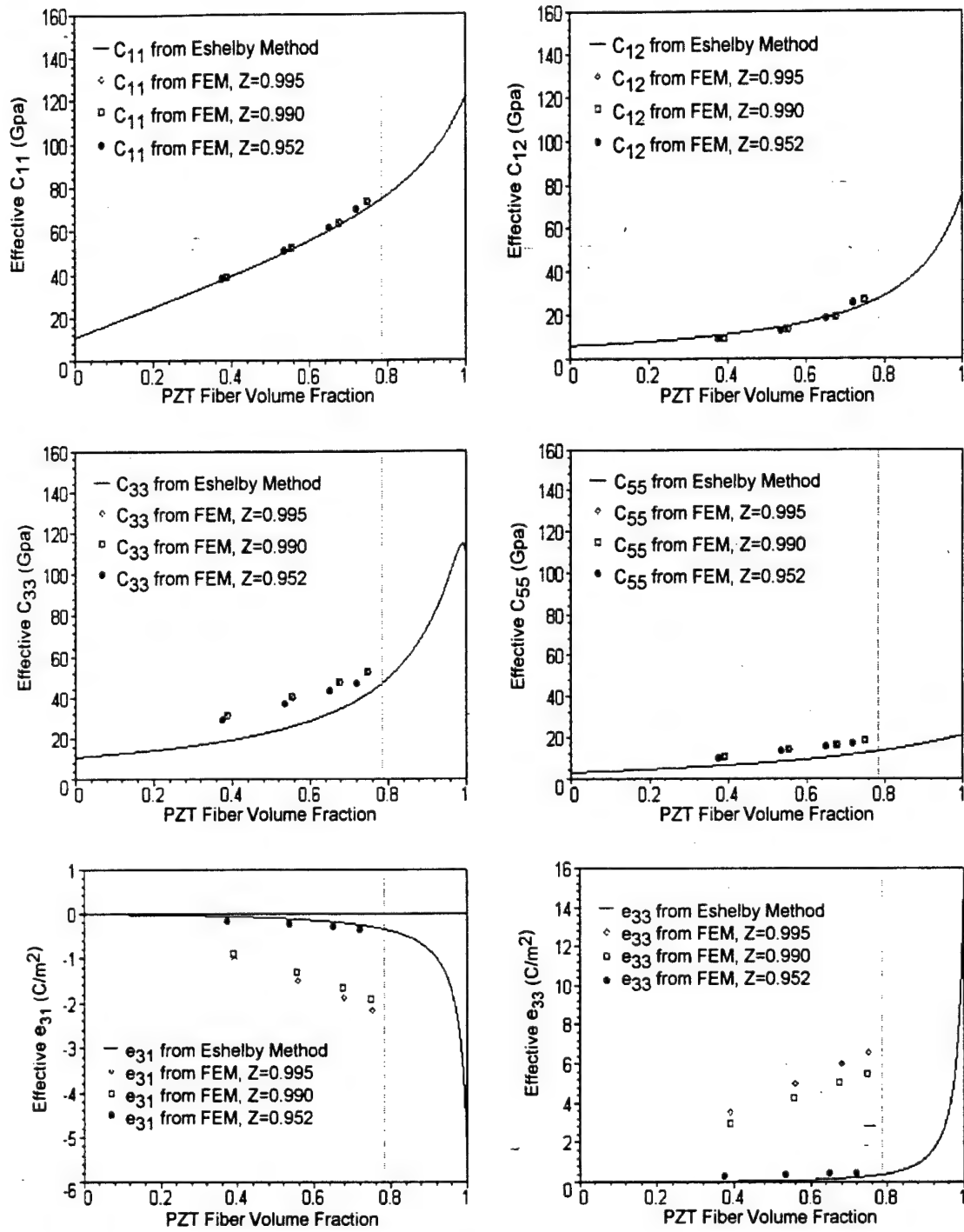
Figure 24. Effective material properties (C_{11}, C_{12}, C_{33}, C_{55}, e_{31}, e_{33}) versus v_f.
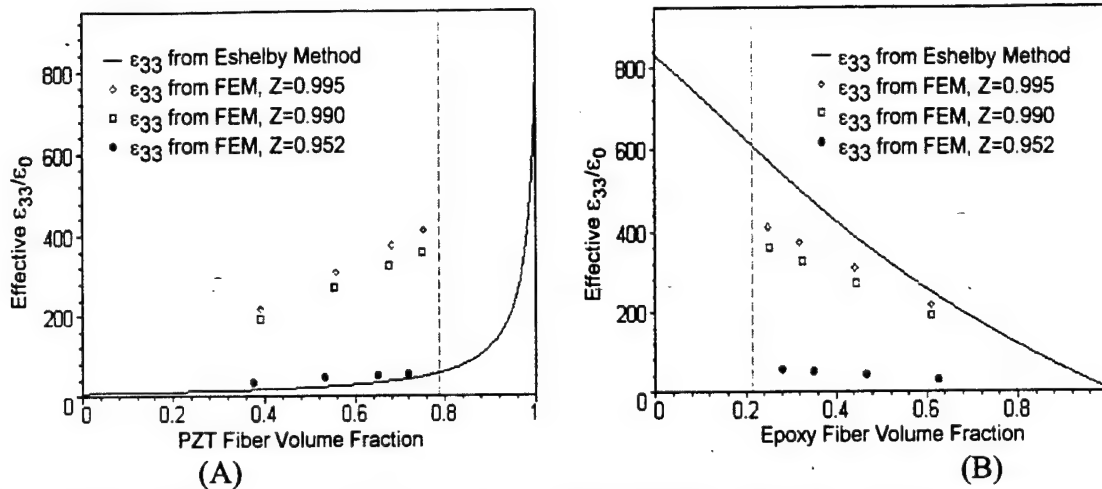
Figure 25. Effective $\varepsilon_{33}/\varepsilon_0$ versus v_f. (A) Compares FEM results to epoxy (white) matrix Eshelby. (B) Compares FEM results to PZT (black) matrix Eshelby (Note: reversal of volume fractions here.)

From examination of Figures 24 and 25 it is seen that the elastic stiffness constants were independent of different Z line fractions and were predicted reasonably well by the micromechanics model. However, for the piezoelectric and dielectric constants a strong dependence on the Z line fraction was observed, but it was also noted that the results trended towards the micromechanics model as the Z line fraction was reduced. Based on this strong dependence of the piezoelectric and dielectric constants on the Z line fraction, it is important to minimize the thickness of the matrix layer between the fibers and the electrode.

Comparison of Figures 25(A) and 25(B) gives insight into the "black matrix/white matrix" issue over which species is actually the matrix at high v_f. The white matrix case gives the general lower limit for all but the highest Z line fraction and the black matrix case gives an upper limit for $Z = 1$.

4.3.   Analysis Of The Piezoelectric Fiber Based FGM Bimorph

Once the effective composite material properties had been found it was then possible to predict the response of a fiber based FGM bimorph. From the analyzed cases, the middle Z line fraction case of $Z = .99$ was chosen at a Y line fractions of $Y = .93, .71, .50$ to represent layers which are all PZT fibers, 2/3 PZT fibers and 1/2 PZT fibers respectively. The actuators as modeled then had three 100 µm thick piezoelectric composite layers on each side of a 25 µm thick brass central electrode with 10 µm thick aluminum electrodes on the surface for a total thickness of 645 µm and a total length of 50 mm. This represents the type of actuators that are currently being fabricated. These were modeled using ANSYS in the 2D plane stress mode which gives displacements that agree well with a full 3D model, but with much less computational effort. The results for this FGM bimorph are compared to a non-FGM bimorph which was dimensionally identical, but had the effective properties for the $Z = .99$, $Y = .93$ layer throughout. Both of these models were subjected to an applied electric field of 500 volts/mm. These results for axial stress, σ_x, are shown below in Figure 26.

27

From these results it is seen that the FGM bimorph is superior with a tip displacement 187 μm, and a maximum axial stress in the piezoelectric layers of 1.27 MPa compared to 175 μm and 2.08 MPa respectively in the non-FGM bimorph. The reduced stresses are likely due to the gradual build up in stress through the three layers of the FGM instead of the much quicker ramp up evidenced in the single layer of the non-FGM samples. The FGM bimorph also compares very favorably with the results for a monolithic FGM monomorph reported elsewhere, as the tip displacement of our FGM bimorph at 500 volts/mm equates to 37.4 μm/cm bending displacement which is superior to the values of 28 μm/cm for the monolithic FGM monomorph.

Initial comparison of the FGM to non-FGM bimorphs may only show a 7% increase in tip deflection, but there are other benefits to the FGM which go along favorably with this increase. Use of the FGM bimorph as opposed to the non-FGM bimorph has led to a reduction in axial stress of 39%. In addition to this, there is the fact that the FGM only uses about 75% of the expensive ceramic piezoelectric fibers required for a non-FGM bimorph of identical thickness, resulting in significant cost savings and reduced weight.
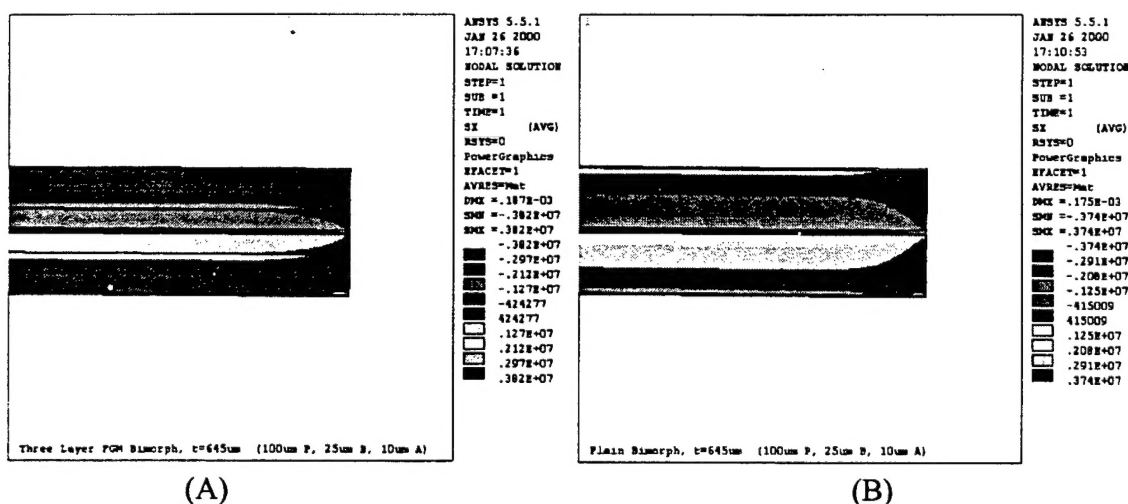

(A)   (B)

Figure 26. Results for axial stress, σ_x. (A) FGM bimorph. (B) non-FGM bimorph.

Further examination of the plots in Figure 26 show that the highest stresses are actually in the aluminum surface electrodes. With this in mind, it will be possible to achieve higher displacements by replacing the aluminum foil with a different electrode material that has a lower stiffness (more flexible), such as a conductive polymer film or conductive epoxy paint.

4.4.   Laser Based Displacement Measurement System

To allow accurate measurement of tip displacement induced in the FGM bimorph a laser based displacement measurement system was designed and fabricated as shown below in Figure 27. The use of a laser based transducer allows for non-contact measurement of tip displacement to allow for true no load displacement measurements. The incorporation of and x-y translation stage into the measurement system allows measurements to be easily taken at various points on the specimen. The data acquisition

and control of the system is done with a Windows based PC. The accuracy of the system is ±3μm in one location and ±5μm when scanning over a surface using the x-y stage.
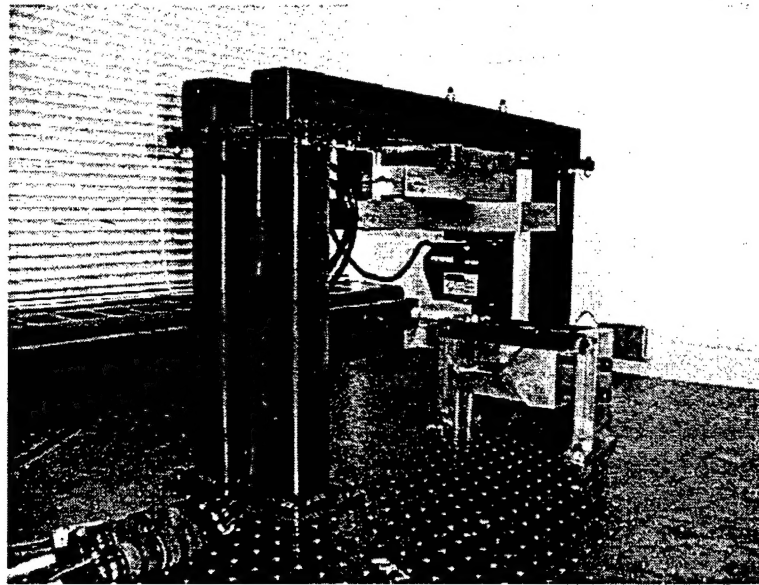

Figure 27. UW Designed and fabricated laser based non-contact displacement measurement system.

5. Concluding Remarks And Future Work

The SS/ZrO$_2$ FGM system exhibited a sudden jump in the fracture resistance K_R, around the percolation threshold point of 30%SS. The fracture resistance of Ni/ZrO$_2$ FGM systems did not exhibit such a sudden jump but rather kind of linear dependence on the volume fraction of the metal phase. The fracture resistance observed in the FGM specimens are explained by two models, residual stress and percolation models focusing on SS/ZrO$_2$ FGM system. The former was accurate in explaining the gradual change in K_R as the volume fraction of the SS metal phase increases up to near the threshold region, 30% SS phase, while the later was reasonably valid in explaining the threshold region. Then the concept of FGM was extended to the case of actuator material design, particularly, piezoelectric laminate with FGM.

The use of FGM in piezoelectric laminates reduces the stress field while increasing the out-of plane displacement as compared with the standard bimorph. The optimization of the material property gradient profile within the FGM laminae provides higher out-of-plane displacement while reducing the stress field. The CLT and 2D elasticity solution of out-of-plane displacement and stress field are close to those obtained by FEM analysis.

The effective material properties for piezoelectric fiber based composites were predicted by using an FEM model of the fiber unit cell which allowed rectangular fiber packing to be accounted for. It was found that the elastic constants are mostly only a function of the overall volume fraction v_f, while the piezoelectric and dielectric constants were more strongly affected by changing the Z line fraction alone than by changes in v_f.

Using these material properties allowed modeling of piezoelectric fiber based FGM bimorph actuators which are under development and indicates that they have advantages over non-FGM bimorphs and also have higher deflection than for other existing monolithic (non-fiber based) FGM monomorphs.

29

Fabrication of such actuators is considered to be a key target of our future work, as well as the validation of the analytical modeling as compared to the experimental data. In conclusion, the concept of FGM is found to be very useful in reducing the stress field at the interface where large mismatch in strain exists, thus inducing large stress field, which can be reduced by using the FGM interface design.

5. References

Almajid, A., Taya, M., and Hudnut, S.(2000). Analysis of Out-of-plane displacement and stress field in a piezocomposite plate with functionally graded microstructure, in press, *Intl. J. Solids Structures*

Bent, A. A., and Hagood, N. W., (1997), "Piezoelectric composites with interdigitated electrodes," *J. Intell. Mat. Sys. and Struct.* **8**, pp. 903-919.

Dunn, M. and Taya, M. (1993a). An analysis of piezoelectric composite materials containing ellipsoidal inhomogeneities, *Proc. Roy. Soc. London* **A443**, 265-287.

Dunn, M. and Taya, M. (1993b). Micromechanics predictions of the effective Electroelastic moduli of piezoelectric composites. *Int. J. solids Structures* **30**,161-175

Eshelby, J. D. (1957). The determination of elastic field of an ellipsoidal inclusion, and related problems, Proc. Royal Soc. London, **A 241**, 376-396

Gibson, R. F. (1994). *Principles of Composite materials and Mechanics,* McGraw Hill

Pagano, N. J. (1969). Exact Solution for Composite Laminates Bending, *J. Composite Materials*, **3**, 398-411

Li, Z., Taya, M. and Dunn, M. (1995). Experimental study of fracture toughness of ceramic/ceramic matrix composite sandwich fracture, *J. Am. Ceramic Soc.*, **78**, 1633-39

Mikata, Y., (2000), "Determination of piezoelectric Eshelby tensor in transversly isotropic piezoelectric solids," *Intl. J. Engrg. Science* **38** [6], pp. 605-641.

Mori, T., and Tanaka, K., (1973), "Average stress in matrix and average elastic energy of materials with misfitting inclusions," *Acta Mettal.* **21**, pp. 571-574.

Taya and Arsenault, (1989). Metal Matrix Composites: Thermomechanical Behavior, *Pergamon Press.*

Taya, M., Lee, J. K., and Mori, T. (1997). Dislocation punching from interfaces in functionally graded materials, *Acta materia*, **45**, 2349-2356

The 1st Annual UW Summer Arts Festival!
July 18 – 22, 2000

The UW Summer Arts Festival is a joyous celebration of the arts including five days of art, cinema, dance, drama, exhibitions, lectures, symposia and more! As a fan of the arts at the University of Washington, you'll want to attend all the exciting performances featured throughout the Festival, including:

The Brechemin Series
featuring performances by the Open Way Quartet, Soni Ventorum, Marc Seales and Friends, and Ronald and Roxanna Patterson with Carmen Pelton and Craig Sheppard

The Chamber Dance Company
Daily performances in the Meany Studio Theatre

UW Drama Department
Daily performances of an exciting new adaptation of Hamlet directed by Susan Finque and featuring performances by UW Drama Department faculty and PATP alumni

Festival Guest Artists
Masada with John Zorn
The Kronos Quartet

Pick up a Festival brochure in the lobby or call (206) 685-6696 for more information. Or send email to artsfest@u.washington.edu.

To purchase tickets call (206) 543-4880.

Visit our web-site at www.summerartsfest.org

JOIN US AND CELEBRATE THE ARTS!